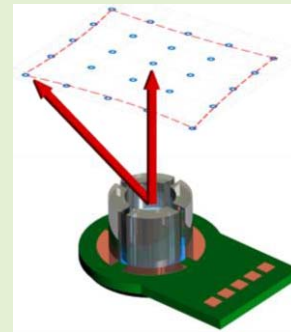


Calibration and Characteristics of an Electrowetting Laser Scanner

Wei Yang Lim¹, Mo Zohrabi, Juliet T. Gopinath¹, *Senior Member, IEEE*, and Victor M. Bright, *Fellow, IEEE*

Abstract—We present a calibration method to correct for fabrication variations and optical misalignment in a two-dimensional electrowetting scanner. These scanners are an attractive option due to being transmissive, nonmechanical, having a large scan angle ($\pm 13.7^\circ$), and low power consumption (μW). Fabrication imperfections lead to non-uniform deposition of the dielectric or hydrophobic layer which results in actuation inconsistency of each electrode. To demonstrate our calibration method, we scan a 5×5 grid target using a four-electrode electrowetting prism and observe a pincushion type optical distortion in the imaging plane. Zemax optical simulations verify that the symmetric distortion is due to the projection of a radial scanning surface onto a flat imaging plane, while in experiment we observe asymmetrical distortion due to optical misalignment and fabrication imperfections. By adjusting the actuation voltages through an iterative Delaunay triangulation interpolation method, the distortion is corrected and saw an improvement in the mean error across 25 grid points from $43 \mu\text{m}$ (0.117°) to $10 \mu\text{m}$ (0.027°). Schematic of a four electrode electrowetting laser scanner used to generate a 25-point grid target.



Index Terms—Calibration, electrowetting, laser scanner, scanning characteristic.

I. INTRODUCTION

LASER scanning technologies have been widely studied and adopted in optical imaging systems that include light detection and ranging (LiDAR) [1]–[3], optical coherence tomography (OCT) [4], microscopy [5]–[7], and optical displays [8]. Depending on the application, mechanical scanners such as micro-electro-mechanical systems (MEMS) mirrors [1], [2] and galvanometric mirrors [9], or non-mechanical scanners operating using spatial light modulators [10], liquid

lenses [11], liquid crystals [12], and acousto-optical modulators [13] have been employed. Despite the various scanning technologies, the choices are limited due to the weight and size requirements. One example is in the brain imaging of awake animals, using a head-mounted microscope [14]. The weight of these systems must be less than 4 g for mice, and the size of the entire package has to be small (less than $\sim 10 \times 10 \text{ mm}^2$) in comparison to the size of the animal [5]–[11]. Electrowetting-based scanners present an attractive alternative for simplifying and miniaturizing optical systems [15]–[18]. They operate based on tilting a single liquid-liquid surface reducing the optical footprint compared to single rotational axis galvanometric mirror [19]. Additionally, the scanner operates in transmission which reduces the optical system complexity, generates large scanning angle of $\pm 13.7^\circ$ [20], has $> 100 \text{ Hz}$ scanning frequency for mm scale devices, while consuming μW of power draw during operation.

Electrowetting is a phenomenon where the contact angle of a liquid is altered by applying an external electric field [21]–[24]. Typically, in an electrowetting device, an electric field is applied between a conductive electrode and a conductive polar liquid, separated by a dielectric layer to prevent unwanted electrochemistry [25]–[27]. Although the commonly used dielectric layer (Parylene) is slightly hydrophobic, to increase the liquid initial contact angle and actuation range [26], [28], [29], an additional hydrophobic coating such as Teflon or Cytop is applied on the surface. Two immiscible liquids, a polar liquid and a non-polar liquid, are typically chosen to provide a refractive index contrast

Manuscript received November 21, 2019; accepted December 4, 2019. Date of publication December 16, 2019; date of current version March 5, 2020. This work was supported in part by the National Science Foundation (NSF) through the Instrument Development for Biological Research (IDBR) under Grant DBI-1353757 and through the Integrative Strategies for Understanding Neural and Cognitive Systems (NCS_FO) under Grant CBET-1631704, in part by the National Institutes of Health (NIH) through the Stimulating Peripheral Activity to Relieve Conditions (SPARC) under Grant 1OT2OD023852 and through the Brain Research through Advancing Innovative Neurotechnologies (BRAIN) under Grant U01 NS099577-02, and in part by the Office of Naval Research (ONR) under Grant N00014-15-1-2739. The associate editor coordinating the review of this article and approving it for publication was Dr. Cheng-Ta Chiang. (*Corresponding author: Wei Yang Lim.*)

W. Y. Lim and V. M. Bright are with the Department of Mechanical Engineering, University of Colorado Boulder, Boulder, CO 80309 USA (e-mail: wei.lim@colorado.edu; victor.bright@colorado.edu).

M. Zohrabi is with the Department of Electrical, Computer, and Energy Engineering, University of Colorado Boulder, Boulder, CO 80309 USA (e-mail: mo.zohrabi@colorado.edu).

J. T. Gopinath is with the Department of Electrical, Computer, and Energy Engineering, University of Colorado Boulder, Boulder, CO 80309 USA, and also with the Department of Physics, University of Colorado Boulder, Boulder, CO 80309 USA (e-mail: julietg@colorado.edu).

Digital Object Identifier 10.1109/JSEN.2019.2959792

and reduce the voltage requirements. Moreover, the densities of these liquids can be selected such that the Bond number $\ll 1$, where surface tension dominates over gravitational or acceleration forces, resulting in a device being insensitive to gravitational distortions. An optical electrowetting device can be in the form of a planar substrate [30], [31] or a vertical device geometry [16], [32], [33]. In the simplest vertical geometry implementation, a single sidewall electrode symmetrically alters the curvature of the liquid-liquid interface which results in an electrically tunable lens [32], [34]–[36]. Multiple sidewall electrodes enable independent control of the contact angle of the liquid meniscus with device walls. For beam steering, a minimum of two electrodes are required to generate a tilt of the meniscus for one-dimensional scanning [16]–[37], whereas devices with at least four electrodes are needed for two-dimensional scanning [18]. The addition of more electrodes increase the control over the liquid-liquid interface enabling optical aberration correction applications [38], [39].

Despite the advantages of electrowetting devices, they are impacted by variations in fabrication, such as differences in dielectric coating thickness, electrode size variations, and hydrophobic layer non-uniformity. Dielectric thickness variations, for example, affect the actuation voltages between drive electrodes, which induce additional curvature on the tilting liquid-liquid interface. These effects are further exacerbated with the fabrication of multiple electrodes. Gaps between actuating electrodes in a multielectrode electrowetting prism create regions of no actuation. Depending on the gap size relative to the size of the device, an optical distortion is manifested across the vicinity or throughout the entirety of the liquid interface. Contact angle measurements while accurate in characterizing the focal power of a single electrode electrowetting lens, are ineffective in predicting the scanning angle of multielectrode configurations because of the non-planar liquid-liquid interface. Consequently, evaluating the scan angle by treating the liquid-liquid interface as a planar surface [17], [37], [40], in a cylindrical geometry yields inaccuracies.

This paper investigates the effects of variations in fabrication tolerances and demonstrates a calibration protocol. We characterized a four-electrode electrowetting prism, by performing a two-dimensional scan of a 25-point grid target. The effects of fabrication variation on the grid target were modeled, by solving the Young-Laplace equation in conjunction with optical design software (Zemax). Finally, we demonstrated an algorithm which successfully compensated position shift errors in a two-dimensional laser scanner through a closed-loop iterative method. The calibration algorithm can be implemented to accommodate for the geometrical distortion, minor optical and fabrication variations, and to provide repeatable scanning with a mean error of 10 μm from the target position.

II. MATERIALS AND METHODS

The electrowetting prism used for these studies is based on a cylindrical 4-mm inner diameter glass tube, capped with a patterned annular ground electrode window on one end and a transparent glass window on the other. The ground electrode provides electrical connection to the polar liquid,

while an Indium Tin Oxide (ITO) coated on the inner walls of a cylindrical glass tube wall functions as the opposing electrode. A 3.7 μm Parylene HT dielectric layer and a Cytop hydrophobic coating layer separate the two electrodes. The thickness of the dielectric layer chosen enabled the device to actuate consistently up to 200 V [20] with a dielectric breakdown voltage calculated at 780 V. The construction of the electrowetting prism begins with the fabrication of the patterned ground window and cylindrical glass tube. The patterned ground window was fabricated through a two-mask layer photolithography process, using a 3" glass wafer. A layer of 300 nm gold and an adhesion layer of 20 nm titanium was sputtered and patterned with a lift off process. Next, a layer of SU-8 photoresist was patterned to separate the ground and vertical electrodes. Individual circular patterned glass windows were then cut using a CO₂ laser cutter. To fabricate the cylindrical glass tube, a 3-D printed shadow mask to create the wall electrode separations necessary for prism actuations, was fitted into a borosilicate tube. The uncovered areas of the tube were sputter-coated with ITO to create the vertical wall electrodes. A layer of Parylene HT was deposited with chemical vapor deposition at Specialty Coating Systems, followed by dip coating a hydrophobic layer (10 % Cytop CTL-809M) at a rate of 1 mm/s.

The two finished parts were then assembled using an ultraviolet (UV)-curable epoxy (Norland UVS-91) and cleaned with an isopropanol alcohol (IPA) and deionized water (DI) rinse (Fig. 1a). The ground and vertical electrodes were electrically connected to a printed circuit board (PCB) using a silver epoxy. DI water and 1-Phenyl-1-cyclohexene (PCH) were chosen as the electrowetting liquids due to their high refractive index contrast, close densities, and fast response [20]. Finally, the device was filled with two liquids before the device was encapsulated using an optical glass window.

A. Experimental Setup

A collimated continuous wave 650 nm laser, with a 1.2 mm beam diameter (full width half maximum, FWHM) was used. The beam was passed through an adaptive lens to focus the spot directly onto the complementary metal-oxide semiconductor (CMOS) camera sensor (Chameleon CM3-U3-13Y3M-CS) (Fig. 2). The four electrode electrowetting device was inserted before the CMOS camera for beam steering. The focusing lens was positioned 75 mm from the electrowetting device's liquid-liquid meniscus, whereas the CMOS camera was 21 mm from the electrowetting device. Throughout the experiment, the optical elements were maintained at the same position and the variable lens kept at the same focusing power. Voltage points were generated using a 32-channel analog output voltage Data Acquisition system (DAQ) (NI-PCIe 6738) and amplified to the required root-mean-square (RMS) value using an 8-channel amplifier (OKO Bipolar HV amplifier).

B. Electrowetting Prism Actuation

A sinusoidal voltage function at 3 kHz with zero voltage offset was used to drive the electrowetting prism. The initial contact angle of the liquid-liquid interface with the device

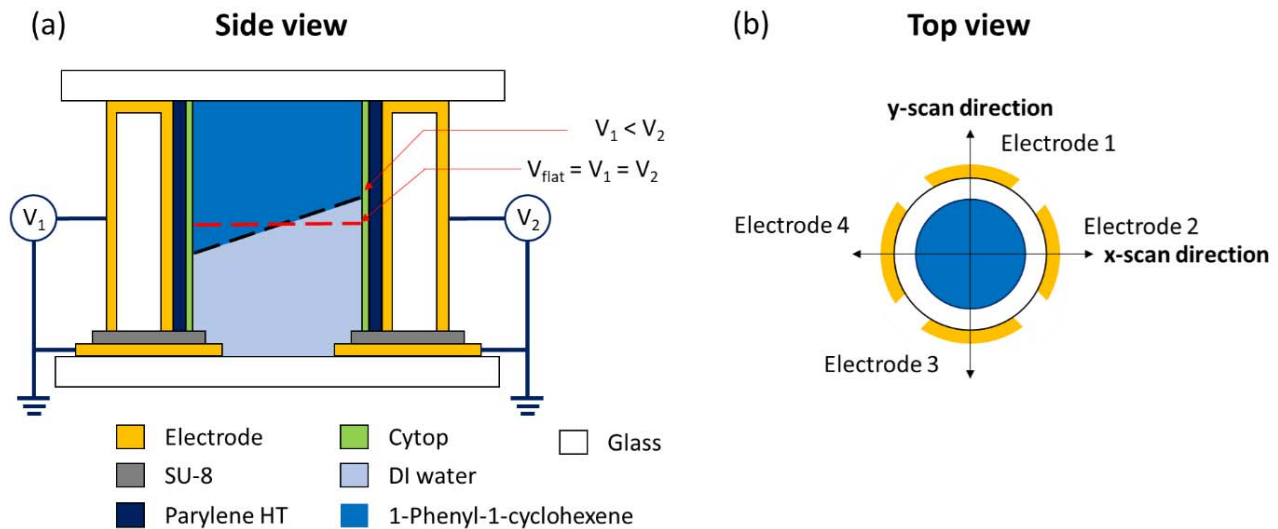


Fig. 1. (a) Cross sectional image of an electrowetting prism. Voltage is applied on the vertical electrode and the ground electrode in electrical contact with the deionized water (DI) water. Parylene HT and SU-8 both were used as dielectric layer, while the Cytop functioned as a hydrophobic layer to increase initial contact angle with sidewall. At 'flat' voltage, V_{flat} , the contact angle of the liquid interface with the device wall is 90° . By tilting the meniscus (liquid-liquid interface) around the flat voltage, beam steering occurs with minimal aberrations. (b) Top view of a four-electrode prism. Opposing electrodes are actuated in sync to achieve scanning in a single direction.

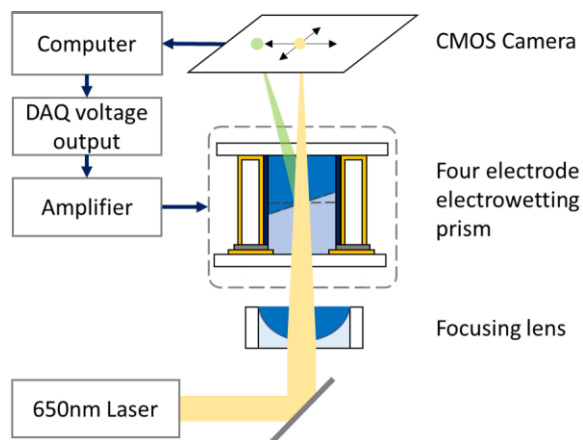


Fig. 2. Schematic of the experimental setup for beam steering calibration using the four electrode electrowetting prism. A 1.2 mm beam diameter (FWHM) was focused onto the CMOS camera and steered using the electrowetting prism. Beam centroids were determined by projecting the intensity profile into its axial components and fitting them to a Gaussian function. The computer calculates the voltage and sends an analog output using a DAQ and an amplifier. The four-electrode prism was used to image a 25-point calibration grid.

sidewall at rest was reported to be 173° with a contact angle-voltage curve which can be tuned to 60° at 170 V as measured in a previous study [20]. When all the electrodes are symmetrically actuated to reach a 90° contact angle, the associating voltage is referred to as the flat voltage (V_{flat}). Steering the prism requires two opposing electrodes to generate a tilt through a difference in voltages. Ideally, the two opposing electrodes will work in tandem, generating opposing contact angles on each side (such as 80° - 100°) around the 90° contact angle keeping the liquid-liquid interface flat and thus minimizing the optical aberrations induced. To achieve beam steering, we actuated the device around a bias voltage (V_{bias})

and introduced a voltage difference (V_{scan}). As an example, a line scan in the x-scan direction for a four-electrode prism, would have the voltage of electrode 2 = $V_{bias} + V_{scan}$ and electrode 4 = $V_{bias} - V_{scan}$ with electrodes 1 and 3 at their flat voltage. By coupling electrodes 1 and 3, and electrodes 2 and 4, we formed two-individual axis for a two-dimensional beam scan.

III. RESULTS AND DISCUSSION

A. Four-Electrode Electrowetting Prism Grid Scan

For two-dimensional beam steering, the electrowetting prism was actuated with $\pm 10 V_{scan}$ at intervals of 5 V on the two axes around $70 V_{bias}$, creating 25 points that form a 5×5 grid. Due to the size of the CMOS sensor, the voltage was limited to $\pm 10 V_{scan}$ or $\sim \pm 2.4^\circ$ of scanning angle. At each voltage point, a time delay of 3 s was used to allow the liquid meniscus to settle to an equilibrium state before the beam spot was captured. The time delay was chosen based on the synchronization timings between the output DAQ and the camera, whereas the liquid response time was ~ 100 ms [20]. The beam centroids were determined by projecting the intensity profile into its axial component and fitting them to a gaussian function. Beam centroids were then normalized with the average maximum distance along the primary axes, rotated, and re-centered with respect to the position at flat voltage (see Fig. 3).

Fig. 3 illustrates the results of two-dimensional scanning of a 5×5 grid using a four-electrode prism with each grid cell division representing $400 \mu\text{m}$. The imaged grid shows a distortion which increased radially from the optical center (illustrated with the red dashed lines) with the maximum deviation of $119 \mu\text{m}$ on the corners. Across the 25 points, the mean error from the normalized grid was measured at $43 \mu\text{m}$ with a standard deviation of $27 \mu\text{m}$. In repeated

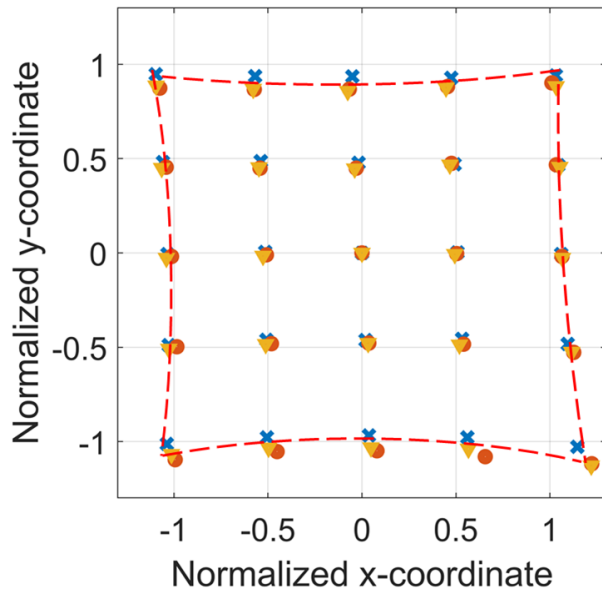


Fig. 3. Two-dimensional grid scanning using a four electrode electrowetting prism actuated with $\pm 10 V_{\text{scan}}$ on 5 V intervals. The experiment was repeated and shown with different markers. Distortion of the grid (illustrated with the dashed line) was seen more prominent further from the optical center and along the diagonal $[(-1,1)$ and $(1,-1)]$. Beam position captured on the CMOS camera is rotated, re-centered, and normalized using the maximum scan distance of the primary axis. Each grid cell represents $400 \mu\text{m}$ in length.

experiments shown with the different markers in Fig. 3, the similar asymmetrical distortion was observed with a more prominent skewness along the diagonal $[(-1,1)$ and $(1,-1)]$. Because the electrowetting prism functions by rotating the liquid interface, the distortion can be attributed to the projection of the radial scanning surface onto a flat sensor surface. This distortion is similar to a pincushion type geometrical distortion and commonly reported in laser spot scanner systems [41]–[44]. In classical pincushion, the distortion is radially dependent with a symmetrical elongation of the corners of a square. In the case of electrowetting scanner shown in Fig. 3, the distortion is asymmetrical which indicates the presence of additional optical distortions in the system. One possibility of the asymmetry is from the unequal actuation voltages due to the fabrication yielding an offset in the center of rotation. Additionally, the induced liquid interface curvature from the gap separation between the electrodes can affect scanning along diagonals (Fig. 1b) leading to the asymmetry. The effect will be enhanced with optical misalignment in the system.

B. Liquid Surface Simulations Results

To evaluate the effect of the electrowetting prism in two-dimensional beam steering, we modeled the optical setup using Zemax optical design software. The liquid-liquid interface of the four-electrode electrowetting prism was simulated by solving Young-Laplace equation [45]–[48]. The equation is derived from energy minimization, and correlates the capillary pressure, surface tension, and principle radii of curvature of the interface between the two liquids. The solution of this equation represents an equilibrium state of the two-liquid interface. The partial differential equation (PDE) toolbox in MATLAB

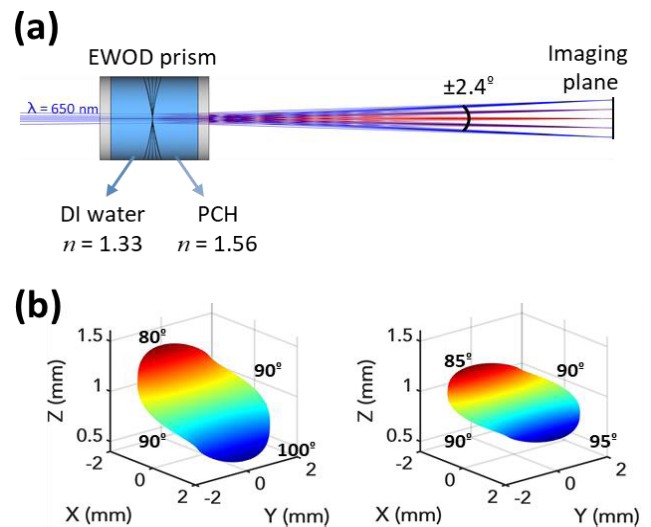


Fig. 4. (a) Schematic of the beam steering setup modeled in Zemax with an electrowetting prism device. A tunable lens is placed before the electrowetting prism (not shown). The focal length of this lens is optimized to generate a focus spot for the scanning beam at the imaging plane, 21 mm from the liquid-liquid meniscus. Outgoing beams with different colors represent scanning configurations for contact angles of $[80^\circ 90^\circ 100^\circ 90^\circ]$, $[85^\circ 90^\circ 95^\circ 90^\circ]$, $[90^\circ 90^\circ 90^\circ 90^\circ]$, $[95^\circ 90^\circ 85^\circ 90^\circ]$, and $[100^\circ 90^\circ 100^\circ 80^\circ]$. Each value corresponds to one of the electrodes on the four-electrode electrowetting prism. (b) Example of the simulated liquid-liquid interface surface, by solving Young-Laplace's equation, for the contact angle configurations of $[80^\circ 90^\circ 100^\circ 90^\circ]$ and $[85^\circ 90^\circ 95^\circ 90^\circ]$.

was implemented to solve the Young-Laplace equation for the 4-mm inner diameter four-electrode electrowetting prism. The steady-state contact angles with the device sidewall were experimentally determined to be 173° with no applied voltage for DI water and PCH liquids combination [20]. Previously, we have validated the simulated surfaces for multielectrode electrowetting device by comparing results to a full 3D computational fluid dynamics simulation based on Laminar two-phase flow in COMSOL Multiphysics [6], [49].

Fig. 4(a) shows the schematic of the Zemax model based on the experimental conditions. The simulated liquid-liquid interface was fitted to 15 Zernike polynomials and the corresponding Zernike coefficient were imported to Zemax. A tunable lens was placed before the electrowetting prism (not shown) to generate a focused spot at the imaging plane. The imaging plane was positioned 21 mm from the liquid-liquid meniscus. The liquid-liquid interface was simulated for 25 contact angle configurations to generate a 5×5 grid pattern. The 5-voltage configuration that generated a one-dimensional scan along the primary axis (x- or y-axis) is presented in Fig. 4(a). For a one-dimensional scan, two of the opposite electrodes were kept at 90° , while the contact angles of the other two electrodes were varied between 80° to 100° degree with step of 5 degrees. Our choice of contact angles generated a $\pm 2.4^\circ$ scan along x and y coordinates. Two examples of the simulated liquid-liquid interface are shown in Fig. 4(b) for contact angles of $[80^\circ 90^\circ 100^\circ 90^\circ]$, $[85^\circ 90^\circ 95^\circ 90^\circ]$, respectively.

Fig. 5(a) depicts the centroids of the focused spots at the imaging plane for 25 configurations with contact angle variations from 80° to 100° with a step of 5 degrees. In our

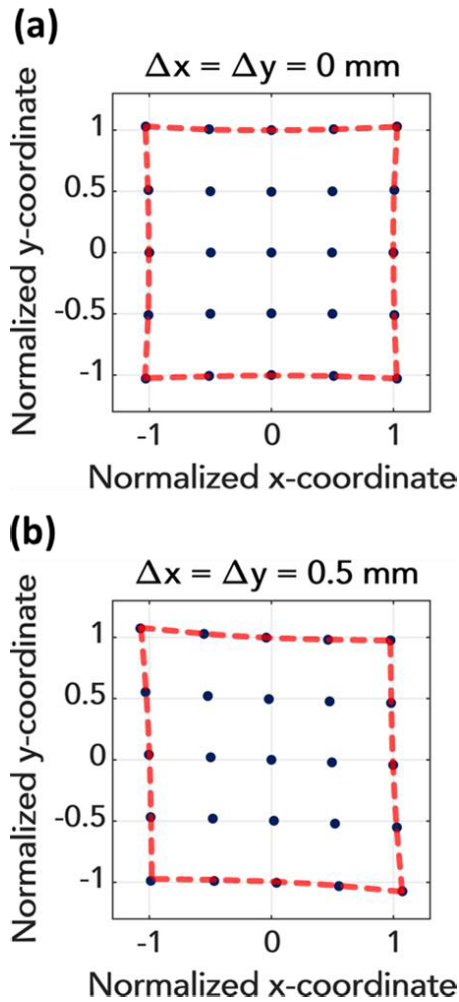


Fig. 5. (a) Centroids of the focused spot at the imaging plane for the 25 simulated contact angle configurations. In this case, the electro-wetting prism is aligned on the optical axis. Pincushion type geometrical distortion such as is present in the grid image. (b) The electro-wetting prism is offset from the optical axis by 0.5 mm in both x and y direction. The resulting simulated asymmetrical induced skewness on the distortion resembled the pattern observed in the experiment.

case, scanning along the x- or y-direction only used two electrodes along those direction, whereas scanning along diagonal direction involved all four electrodes. The centroids are normalized with respect to the maximum distance along the primary axis (x and y). The spot diagram centroid exhibits geometrical deformation similar to a pincushion type distortion reported in the other laser scanner studies [41]–[44]. The red dashed lines were drawn at the edge of the grid scan to clarify the pincushion type effect [see Fig. 5(a)]. The optical distortion is a result of focusing to a radial scanning surface and imaging this onto a flat surface. In effect, the image is magnified toward the periphery as seen here. A surface with only tilt was also simulated in place of the liquid-liquid meniscus to contrast the effects from the scanning projection on a planar surface. Scanning with all four electrodes did not add any significant distortion to the image as the initial curvature of the scanning surface was minimal. The origin of the geometrical distortion is thereby synonymous with other laser scanners.

To further understand the two-dimensional scanning pattern observed in the experiment, we offset the electro-wetting prism significantly with respect to the optical axis by 0.5 mm in both x and y directions. The centroids of the focused spots at the imaging plane were plotted in Fig. 5(b). The distortion was skewed toward one direction due to the asymmetry introduced by the electro-wetting prism. This confirms our experimental observation that electro-wetting prism misalignment can cause asymmetrical distortion in the imaging plane. In addition, any fabrication imperfections can result in dissimilarity between the four electrodes. Such an asymmetry in the operating device produces a skewed distortion in the imaging plane. One can effectively compensate for these interdependences as well as fabrication shortcomings by varying the applied voltages on each electrode iteratively (by varying the contact angles) which is explored in the following section.

C. Correction Algorithm

Although the distortion can be minimized through the refinement of the fabrication processes, it is more effective to compensate through individual calibration of the devices. As the response time of the electro-wetting system is limited by the liquid dynamics, around 100 ms when actuated from rest [20], algorithms which require large amount of iterations before converging on a solution would be time inefficient. We explored a linear interpolation method to compensate for the distortions in the four-electrode prism through voltage adjustments. A closed loop system was implemented by collecting the beam position using the CMOS camera and actuating the device using a PCIe analog output DAQ on a computer.

To setup the electro-wetting scanner for the calibration, a computer was used to send the actuation voltages and read positional data of the beam using the CMOS camera. A 5×5 grid target was generated to estimate the error from the distortions and serve as the initial datapoints used for interpolation. The correction algorithm calculates the necessary voltage using a linear interpolation method based on the Delaunay triangulation method. An example of the interpolation method is illustrated in Fig. 6. The method uses the voltages of nearest neighboring points to interpolate a new voltage [‘•’ marker in Fig. 6(a)]. In the next iteration, the database is updated, and the new voltage mesh becomes finer, improving the accuracy of its prediction shown in Fig. 6(b). Starting from a corner, the algorithm optimizes the error for each point of the 5×5 grid. Two separate voltage meshes were used for each axis of scanning. At the end of each iteration, positional error from the target coordinates was reevaluated to determine whether the error was within the specified margins of 10% of the grid or $40 \mu\text{m}$. If the error falls outside the predefined margin, the process is iterated until the solution converges, after which the algorithm moves to the next neighboring point. Since the speed of the calibration process is limited by the liquid dynamics, this method is chosen to minimize the travel of the liquid meniscus, reducing the time required for oscillation dampening. In the scenario where the target position laid beyond any existing data point, especially

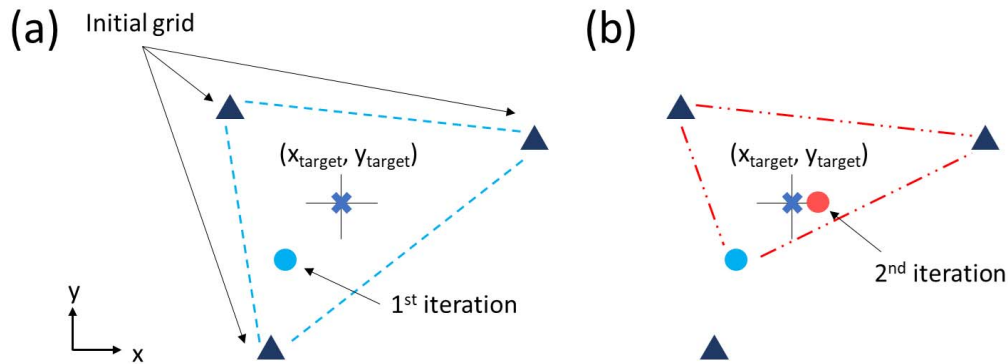


Fig. 6. (a) Illustration of the calibration algorithm optimizing the error of a single point. The 'x' markers indicate the target position, '▲' markers indicate the points generated in the initial 5×5 grid, and the '●' markers indicate the iterations attempts. The algorithm optimizes the target point by using a linear Delaunay triangulation method to interpolate voltage values from the nearest neighboring '▲' points. (a) The first iteration interpolates using the voltages from the initial grid points generating a new point within the boundary. (b) In the second iteration, the interpolation uses the two of the '▲' points and the '●' from the first iteration instead. With a finer mesh of datapoints, the algorithm converges to a solution after a few iterations. On average, 22 points out of the 25 points converge to within the 10% ($40 \mu\text{m}$) error during the first attempt with a total of 31 iterations to reach a solution.

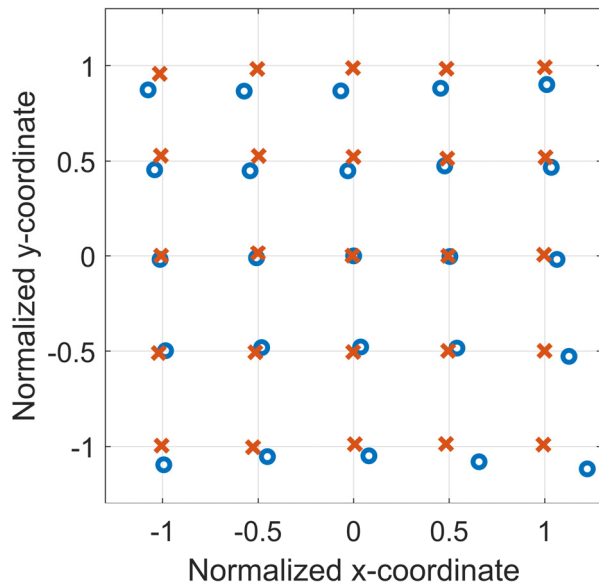


Fig. 7. The initial uniformly voltage spaced grid (o markers) versus a scan after the correction algorithm (x markers) has been applied. Mean position error across the 25 grid points was calculated to have reduced from $43 \mu\text{m}$ to $10 \mu\text{m}$.

for large distortions at the edge of the grid, a random point was generated within the maximum boundary of a unit cell to assist the algorithm in the next interpolation.

The algorithm used a list of datapoints consisting of the initial 25-point grid and the iteration attempts to generate a final uniformly spaced grid (shown in Fig. 7). On average, ~ 22 points out of the 25-grid points across three tests converged to within $40 \mu\text{m}$ or 10% of the distance of a single grid in the first iteration. The geometric distortion and the asymmetric skewness were successfully corrected with the mean error across the entire grid reduced from $43 \mu\text{m}$ (0.117°) to $10 \mu\text{m}$ (0.027°) and a standard deviation improvement from $27 \mu\text{m}$ to $5 \mu\text{m}$. The standard deviation in an uncalibrated device was larger due to the presences of optical misalignment, fabrication inaccuracies, and geometrical distortions. Optical misalignment and fabrication variability

asymmetrically enhance the steering angle in one direction, while reducing the opposing direction which increased the spread of the measurement. Although efforts have been made to optically align the device below the offset conditions used in the simulations, the distortion remains evident in the scan pattern indicating possible fabrication variability. The improvement of the standard deviation reaffirms the calibration algorithm as an effective alternative in compensating for experimental and fabrication variability. Final accuracy and precision of the device will be determined by effects such as charge trapping within the dielectric layer [22], [50], [51] or surface roughness [52] which introduce contact angle tuning hysteresis.

An average of 31 total iterations was required across the three repetitions before all 25 points converged to within 10% error. It was observed that most of the exceptions were situated on the boundary of the grid, which lacked neighboring data points to accurately estimate the correct voltage. In scenarios where the solution failed to converge, the cause was found to be associated with non-uniform coating of the hydrophobic layer. This led to a localized pinning of the liquid meniscus which distorted all neighboring interpolation values. With a functional device without any local pinning effects, the final uniformly spaced grid target was achieved through a minor voltage adjustment of 0.543 V across the three runs to compensate for the distortions. The voltage required to actuate the device over time did not experienced significant drift over the course of the experiment. Repeated measurements with a purified PCH solution with a constant voltage in an uncalibrated one-dimensional scan saw less than 0.08° drift at large steering angles of $\pm 8^\circ$ in a time span of 40 minutes.

When the calibration algorithm was repeated using a tighter calibration error margin of $20 \mu\text{m}$, a significant increase in the iterations was observed with most points failing to converge. The calculated error in each iteration oscillated above the error threshold and in some cases diverged from the target solution. Since the calibration error margin is approaching the precision of the measurement, the calibration algorithm encounters issues with the overfitting of the data.

IV. CONCLUSIONS

We have demonstrated a calibration algorithm for an electrowetting laser scanner which can produce a repeatable two-dimensional scan which reduced mean positional errors across 25 points from $43\ \mu\text{m}$ (0.117°) to $10\ \mu\text{m}$ (0.027°) in a calibrated device. Two-dimensional scanning using a four-electrode prism of a 25-point grid pattern revealed a pincushion type optical distortion often seen in a two-dimensional laser scanner. Liquid surface simulation coupled with Zemax showed that the distortion was induced as an artifact of projecting a focused radial scanning surface onto a flat imaging surface. The asymmetry of the distortion from the experimental data was caused by the combination of the optical alignment and non-equal actuations of electrodes due to fabrication variances. Finally, the geometric distortion, optical misalignment, and fabrication variance were successfully corrected using minor voltage adjustments based on a linear interpolation method of the neighboring voltages.

ACKNOWLEDGMENT

The authors would like to thank Dr. O. Supekar, from the University of Colorado Boulder, for the insightful suggestions and Hans Green of the instrument shop, from the University of Colorado Boulder, for cutting the cylindrical tubes to be later assembled into lenses.

REFERENCES

- [1] C. Niclass *et al.*, "Design and characterization of a 256×64 -pixel single-photon imager in CMOS for a MEMS-based laser scanning time-of-flight sensor," *Opt. Express*, vol. 20, no. 11, 2012, Art. no. 011863.
- [2] A. Kasturi, V. Milanovic, B. H. Atwood, and J. Yang, "UAV-borne LIDAR with MEMS mirror-based scanning capability," *Proc. SPIE*, vol. 9832, May 2016, Art. no. 98320M.
- [3] M. Zohrabi, W. Y. Lim, R. H. Cormack, O. D. Supekar, V. M. Bright, and J. T. Gopinath, "Lidar system with nonmechanical electrowetting-based wide-angle beam steering," *Opt. Express*, vol. 27, no. 4, p. 4404, 2019.
- [4] Y. Pan, H. Xie, and G. K. Fedder, "Endoscopic optical coherence tomography based on a microelectromechanical mirror," *Opt. Lett.*, vol. 26, no. 24, p. 1966, 2001.
- [5] W. Zong *et al.*, "Fast high-resolution miniature two-photon microscopy for brain imaging in freely behaving mice," *Nature Methods*, vol. 14, pp. 713–719, May 2017.
- [6] O. D. Supekar *et al.*, "Two-photon laser scanning microscopy with electrowetting-based prism scanning," *Biomed. Opt. Express*, vol. 8, no. 12, p. 5412, 2017.
- [7] E. B. Brown *et al.*, "In vivo measurement of gene expression, angiogenesis and physiological function in tumors using multiphoton laser scanning microscopy," *Nat. Med.*, vol. 7, no. 7, pp. 864–868, 2001.
- [8] M. H. Kiang, O. Solgaard, K. Y. Lau, and R. S. Müller, "Polysilicon optical microscanners for laser scanning displays," *Sens. Actuators, A Phys.*, vol. 70, nos. 1–2, pp. 195–199, 1998.
- [9] B. Jaeggi *et al.*, "Ultra-high-precision surface structuring by synchronizing a galvo scanner with an ultra-short-pulsed laser system in MOPA arrangement," *Proc. SPIE*, vol. 8243, Feb. 2012, Art. no. 82430K.
- [10] E. Hällstig, L. Sjöqvist, and M. Lindgren, "Intensity variations using a quantized spatial light modulator for nonmechanical beam steering," *Opt. Eng.*, vol. 42, no. 3, p. 613, 2003.
- [11] B. N. Ozbay *et al.*, "Miniaturized fiber-coupled confocal fluorescence microscope with an electrowetting variable focus lens using no moving parts," *Opt. Lett.*, vol. 40, no. 11, p. 2553, 2015.
- [12] D. P. Resler, D. S. Hobbs, R. C. Sharp, L. J. Friedman, and T. A. Dorschner, "High-efficiency liquid-crystal optical phased-array beam steering," *Opt. Lett.*, vol. 21, no. 9, pp. 689–691, 1996.
- [13] G. R. B. E. Römer and P. Bechtold, "Electro-optic and acousto-optic laser beam scanners," *Phys. Procedia*, vol. 56, pp. 29–39, 2014.
- [14] T. Liu, M. Rajadhyaksha, and D. L. Dickensheets, "MEMS-in-the-lens architecture for a miniature high-NA laser scanning microscope," *Light Sci. Appl.*, vol. 8, no. 1, p. 59, 2019.
- [15] N. R. Smith, H. Linlin, J. Zhang, and J. Heikenfeld, "Fabrication and demonstration of electrowetting liquid lens arrays," *J. Display Technol.*, vol. 5, no. 11, pp. 411–413, Nov. 2009.
- [16] S. Terrab, A. M. Watson, C. Roath, J. T. Gopinath, and V. M. Bright, "Adaptive electrowetting lens-prism element," *Opt. Express*, vol. 23, no. 20, 2015, Art. no. 25838.
- [17] C. Enrico Clement and S. Y. Park, "High-performance beam steering using electrowetting-driven liquid prism fabricated by a simple dip-coating method," *Appl. Phys. Lett.*, vol. 108, no. 19, 2016, Art. no. 191601.
- [18] D. Kopp, L. Lehmann, and H. Zappe, "Optofluidic laser scanner based on a rotating liquid prism," *Appl. Opt.*, vol. 55, no. 9, p. 2136, 2016.
- [19] M. Niesten, R. Sprague, and J. Miller, "Scanning laser beam displays," *Proc. SPIE*, vol. 7001, May 2008, Art. no. 70010E.
- [20] W. Y. Lim, O. D. Supekar, M. Zohrabi, J. T. Gopinath, and V. M. Bright, "Liquid combination with high refractive index contrast and fast scanning speeds for electrowetting adaptive optics," *Langmuir*, vol. 34, no. 48, pp. 14511–14518, 2018.
- [21] F. Mugele and J.-C. Baret, "Electrowetting: From basics to applications," *J. Phys. Condens. Matter*, vol. 17, no. 28, pp. R705–R774, 2005.
- [22] H. J. J. Verheijen and M. W. J. Prins, "Reversible electrowetting and trapping of charge: Model and experiments," *Langmuir*, vol. 15, no. 20, pp. 6616–6620, 1999.
- [23] V. Peykov, A. Quinn, and J. Ralston, "Electrowetting: A model for contact-angle saturation," *Colloid Polym. Sci.*, vol. 278, no. 8, pp. 789–793, 2000.
- [24] T. B. Jones, J. D. Fowler, Y. S. Chang, and C. J. Kim, "Frequency-based relationship of electrowetting and dielectrophoretic liquid microactuation," *Langmuir*, vol. 19, no. 18, pp. 7646–7651, 2003.
- [25] B. Berge, "Électrocapillarité et mouillage de films isolants par l'eau," *Comp. Rendus De L'Academie Des Sci. Paris, Serie*, vol. 317, pp. 157–163, 1993.
- [26] W. C. Nelson and C.-J. Kim, "Droplet actuation by electrowetting-on-dielectric (EWOD): A review," *J. Adhes. Sci. Technol.*, vol. 26, pp. 1747–1771, May 2012.
- [27] J. H. Chang, D. Y. Choi, S. Han, and J. J. Pak, "Driving characteristics of the electrowetting-on-dielectric device using atomic-layer-deposited aluminum oxide as the dielectric," *Microfluid. Nanofluidics*, vol. 8, no. 2, pp. 269–273, 2010.
- [28] J. K. Lee, K. W. Park, H. R. Kim, and S. H. Kong, "Dependence of dielectric layer and electrolyte on the driving performance of electrowetting-based liquid lens," *J. Inf. Disp.*, vol. 11, no. 2, pp. 84–90, 2010.
- [29] S. Chevalliot, S. Kuiper, and J. Heikenfeld, "Experimental validation of the invariance of electrowetting contact angle saturation," *J. Adhes. Sci. Technol.*, vol. 26, pp. 12–17, Mar. 2012.
- [30] T. Krupenkin, S. Yang, and P. Mach, "Tunable liquid microlens," *Appl. Phys. Lett.*, vol. 82, no. 3, pp. 316–318, Jan. 2003.
- [31] A. Shahini *et al.*, "Toward individually tunable compound eyes with transparent graphene electrode," *Bioinspiration Biomimetics*, vol. 12, no. 4, 2017, Art. no. 046002.
- [32] S. Kuiper and B. H. W. Hendriks, "Variable-focus liquid lens for miniature cameras," *Appl. Phys. Lett.*, vol. 85, no. 7, pp. 1128–1130, Aug. 2004.
- [33] L. Hou, J. Zhang, N. Smith, J. Yang, and J. Heikenfeld, "A full description of a scalable microfabrication process for arrayed electrowetting micropisms," *J. Micromech. Microeng.*, vol. 20, no. 1, 2010, Art. no. 015044.
- [34] B. Berge and J. Peseux, "Variable focal lens controlled by an external voltage: An application of electrowetting," *Eur. Phys. J.*, vol. 3, no. 2, pp. 159–163, Oct. 2000.
- [35] C. U. Murade, D. van der Ende, and F. Mugele, "High speed adaptive liquid microlens array," *Opt. Express*, vol. 20, no. 16, 2012, Art. no. 018180.
- [36] A. M. Watson, K. Dease, S. Terrab, C. Roath, J. T. Gopinath, and V. M. Bright, "Focus-tunable low-power electrowetting lenses with thin parylene films," *Appl. Opt.*, vol. 54, no. 20, pp. 6224–6229, 2015.
- [37] N. R. Smith, D. C. Abeyasinghe, J. W. Haus, and J. Heikenfeld, "Agile wide-angle beam steering with electrowetting micropisms," *Opt. Express*, vol. 14, no. 14, p. 6557, 2006.
- [38] D. Kopp and H. Zappe, "Tubular astigmatism-tunable fluidic lens," *Opt. Lett.*, vol. 41, no. 12, pp. 2735–2738, 2016.

- [39] N. C. Lima, K. Mishra, and F. Mugele, "Aberration control in adaptive optics: A numerical study of arbitrarily deformable liquid lenses," *Opt. Express*, vol. 25, no. 6, p. 6700, 2017.
- [40] J. Cheng and C. L. Chen, "Adaptive beam tracking and steering via electrowetting-controlled liquid prism," *Appl. Phys. Lett.*, vol. 99, no. 19, pp. 1–4, 2011.
- [41] J. Xie, S. Huang, Z. Duan, Y. Shi, and S. Wen, "Correction of the image distortion for laser galvanometric scanning system," *Opt. Laser Technol.*, vol. 37, no. 4, pp. 305–311, 2005.
- [42] D. Wang, P. Liang, S. Samuelson, H. Jia, J. Ma, and H. Xie, "Correction of image distortions in endoscopic optical coherence tomography based on two-axis scanning MEMS mirrors," *Biomed. Opt. Express*, vol. 4, no. 10, p. 2066, 2013.
- [43] Y. Li, "Beam deflection and scanning by two-mirror and two-axis systems of different architectures: A unified approach," *Appl. Opt.*, vol. 47, no. 32, p. 5976, 2008.
- [44] T. Sidler, "Study of the beam path distortion profiles generated by a two-axis tilt single-mirror laser scanner," *Opt. Eng.*, vol. 42, no. 4, p. 1048, 2003.
- [45] F. Robert, *Equilibrium Capillary Surfaces*. New York, NY, USA: Springer-Verlag, 2012.
- [46] S.-L. Lee and C.-F. Yang, "Numerical simulation for meniscus shape and optical performance of a MEMS-based liquid micro-lens," *Opt. Express*, vol. 16, no. 24, pp. 19995–20007, 2008.
- [47] T. Sarpkaya, "Vorticity, free surface, and surfactants," *Annu. Rev. Fluid Mech.*, vol. 28, no. 1, pp. 83–128, 1996.
- [48] S.-L. Lee and H.-D. Lee, "Evolution of liquid meniscus shape in a capillary tube," *J. Fluids Eng.*, vol. 129, no. 8, p. 957, 2007.
- [49] M. Zohrabi *et al.*, "Numerical analysis of wavefront aberration correction using multielectrode electrowetting-based devices," *Opt. Express*, vol. 25, no. 25, p. 31451, 2017.
- [50] M. K. Kilaru, J. Heikenfeld, G. Lin, and J. E. Mark, "Strong charge trapping and bistable electrowetting on nanocomposite fluoropolymer: BaTiO₃ dielectrics," *Appl. Phys. Lett.*, vol. 90, no. 21, pp. 23–25, 2007.
- [51] D. Thomas *et al.*, "Charge injection in dielectric films during electrowetting actuation under direct current voltage," *Thin Solid Films*, vol. 590, pp. 224–229, Sep. 2015.
- [52] M. E. R. Shanahan, "Simple theory of 'stick-slip' wetting hysteresis," *Langmuir*, vol. 11, no. 3, pp. 1041–1043, 1995.



Wei Yang Lim received the B.S. degree in mechanical engineering from North Dakota State University and the M.S. degree in nanotechnology from the University of Pennsylvania. He is currently pursuing the Ph.D. degree in mechanical engineering with a research focus on electrowetting tunable optical systems.



Mo Zohrabi received the B.S. degree in solid state physics from the University of Tehran, the M.S. degree in optics from the Institute for Advanced Studies in Basic Sciences, and the Ph.D. degree in atomic, molecular, and optical physics from Kansas State University. From 2014 to 2017, he worked as a Postdoctoral Researcher at the James R. Macdonald Laboratory and the University of Colorado Boulder. From 2017 to 2019, he worked as a Research Associate and a Senior Research Associate at the University of Colorado Boulder. His research has resulted in 33 publications appearing in peer-reviewed journals, including *Nature Communications*, *Physical Review Letters*, and *Optics Express*. His research focuses on implementation of electrowetting devices in optical systems, integrated photonics, nonlinear optics, and ultrafast optics.



Juliet T. Gopinath received the B.S. degree in electrical engineering from the University of Minnesota and the S.M. and Ph.D. degrees in electrical engineering from MIT. From 2005 to 2009, she worked as a member of Technical Staff at the MIT Lincoln Laboratory. She is the Alfred T. and Betty E. Look Endowed Associate Professor of Electrical, Computer, and Energy Engineering with the College of Engineering and Applied Sciences, University of Colorado Boulder. She has authored or coauthored 55 peer-reviewed journal articles and over 65 conference proceedings. Her research focuses on adaptive optical devices, integrated photonics, ultrafast optics, and nonlinear microscopy, including orbital angular momentum. She was a member of the IEEE Photonics Society Publications Council from 2017 to 2018, and an Associate Director for the CUBit Quantum Initiative in 2019. She served as an Associate Editor for the IEEE PHOTONICS JOURNAL from 2011 to 2017.



Victor M. Bright (F'15) received the B.S.E.E. degree from the University of Colorado Denver in 1986, and the M.S. and Ph.D. degrees from the Georgia Institute of Technology in 1989 and 1992, respectively. He is a Professor of Mechanical Engineering with the College of Engineering and Applied Science, University of Colorado Boulder. From 2005 to 2007, he was the Associate Dean for Research at the College of Engineering, and from 2009 to 2013, he was the Department Chair of Mechanical Engineering. He is currently the Assistant Vice Chancellor for Research at the University of Colorado Boulder. Prior to joining the University of Colorado, he was a Professor with the Department of Electrical and Computer Engineering, Air Force Institute of Technology, Wright-Patterson Air Force Base, OH, USA, from 1992 to 1997. In 2004, he was a Visiting Professor with the Swiss Federal Institute of Technology (ETH-Zurich), Switzerland. He has over 300 publications in the field of sensors and microsystems and has advised over 50 Ph.D. and M.S. graduate students during his career. His research activities include nano- and micro-electro-mechanical systems (N/MEMS), silicon micromachining, microsensors/microactuators, optical, magnetic and RF microsystems, atomic-layer deposited materials, N/MEMS reliability, and N/MEMS packaging. He is a Fellow of the ASME. He was the General Co-Chair of the IEEE MEMS 2005 International Conference, Miami, FL, USA. He also served on the Technical Program Committees for the Transducers'03, Transducers'07, Transducers'13, IEEE/LEOS Optical MEMS 2003–2005, and Hilton Head 2008 Solid-State Sensors and Actuators Workshop. He has taught a Short Course on MEMS Packaging at Transducers'03 and Transducers'05. He was the General Technical Chair for the Transducers 2015 International Conference, Anchorage, AK. From 2005 to 2018, he was an Editor of the Micromechanics Section of the *Journal of Sensors and Actuators A: Physical* (Elsevier).